BioOne DIGITAL LIBRARY

Optimization of Data Collection and Refinement of Post-processing Techniques for Maritime Canada's First Shallow Water Topographic-bathymetric Lidar Survey

Authors: Webster, Timothy, McGuigan, Kevin, Crowell, Nathan, Collins, Kate, and MacDonald, Candace

Optimization of Data Collection and Refinement of Post-processing Techniques for Maritime Canada's First Shallow Water Topographic-bathymetric Lidar Survey

Timothy Webster[†], Kevin McGuigan[†], Nathan Crowell[†], Kate Collins[†], and Candace MacDonald[†]

[†]Applied Geomatics Research Group
Nova Scotia Community College
Middleton, NS B0M 1M0, Canada

www.cerf-jcr.org

www.JCRonline.org

ABSTRACT

Webster, T.; McGuigan, K.; Crowell, N.; Collins, K., and MacDonald, C., 2016. Optimization of data collection and refinement of post-processing techniques for Maritime Canada's first shallow water topographic-bathymetric lidar survey. *In*: Brock, J.C.; Gesch, D.B.; Parrish, C.E.; Rogers, J.N., and Wright, C.W. (eds.), *Advances in Topobathymetric Mapping, Models, and Applications. Journal of Coastal Research*, Special Issue, No. 76, pp. 31–43. Coconut Creek (Florida), ISSN 0749-0208.

An airborne topographic-bathymetric lidar survey was conducted for five coastal study sites in Maritime Canada in fall 2014 using the shallow water Leica AHAB Chiroptera II sensor. The sensor utilizes near-infrared (NIR) and green lasers to map topography, water surface, and bathymetry, and is equipped with a 60 MPIX camera, which results in 5-cm resolution color and NIR orthophotos. Depth penetration of the lidar sensor is limited by water clarity, and because the coastal zone is vulnerable to reduced water clarity/increased turbidity due to fine-grained sediment suspended by wind-induced waves, several techniques were employed to obtain maximum depth penetration of the sensor. These included monitoring wind speed, direction, and water clarity at study locations, surveying a narrow pass of the study area to assess depth penetration, and quickly adapting to changing weather conditions by altering course to an area where water clarity was less affected by wind-induced turbidity. These techniques enabled 90% depth penetration at all five of the shallow embayments surveyed and up to 6 m depth penetration in the exposed coastal region. Synchronous ground truth surveys were conducted to measure water depth and clarity and seabed cover during the surveys. GPS checkpoints on land indicated that the topographic lidar had an accuracy of better than 10 cm RMSE in the vertical. The amplitude of the green laser bathymetric returns provides information on bottom type and can be useful for generating maps of vegetation distribution. However, these data are not automatically compensated for water depth attenuation and signal loss in post-processing, which results in difficulties in interpreting the amplitude imagery derived from the green laser. An empirical approach to generating a depth-normalized amplitude image which is merged with elevation derivatives to produce a 2-m resolution map product that is easily interpreted by end users is presented. An eelgrass distribution model was derived from the bathymetric elevation parameters with 80% producer's accuracy.

ADDITIONAL INDEX WORDS: *Eelgrass, lidar seabed reflectance, depth normalization, seabed classification.*

INTRODUCTION

The coastal zone of Maritime Canada is estimated to be >11,000 km (Sebert and Monroe, 1972, 1:250,000 scale). The coast plays a significant role in the economy of Maritime Canada through tourism, recreation, fishing, aquaculture, and industry (Fisheries and Oceans Canada, 2008) and has the potential to support more economic development (Tedsen *et al.*, 2014). As the global climate changes, Maritime Canada's coast is at risk from rising sea level and increased erosion (Forbes *et al.*, 2009; Peltier, 2004; Rahmstorf *et al.*, 2007; Shaw *et al.*, 1998; Stocker *et al.*, 2013), and ecosystems are threatened by declining eelgrass and fish habitat (AMEC Earth & Environmental, 2007; Fisheries and Oceans Canada, 2009; Hanson, 2004). The requirement for accurate and detailed mapping of shorelines, nearshore bathymetry, and coastal ecosystems is imperative in order to protect existing infrastructure and vulnerable habitat from erosion and flooding, plan for future sustainable development, and make sound decisions with regard to controversial activities that support economic growth, such as aquaculture and energy infrastructure.

Mapping the coastal zone using traditional aerial photography or boat-based echo sounder methods can be expensive, time consuming, and challenging in shallow water (Elhassan, 2015; Waddington and Hart, 2003). Airborne topographic-bathymetric (topobathy) lidar overcomes these challenges by utilizing a near-infrared (NIR) laser for topographic data collection and a green laser for bathymetric data collection to generate high-resolution, continuous land-sea digital elevation models (DEMs) and aerial orthophoto mosaics. Although shallow water topobathymetric lidar (TBL) sensors are relatively new, the deeper water airborne laser bathymetry (ALB) sensors have been used to demonstrate a variety of coastal research applications ranging from bottom classification and fine-detail bathymetric mapping to coastal management; many of these uses of ALB are summarized in Brock and Purkis (2009). ALB has been demonstrated in

Maritime Canada by Collin, Archambault, and Long (2011) and Collin, Long, and Archambault (2012, 2011) in the Gulf of St. Lawrence along the Quebec coastline. These authors used the Optech SHOALS 1000 system to survey a section of the coastal zone and derived habitat classes from a combination of elevation and reflectance data. Depth-derived variables from ALB data have been used successfully to determine sea floor rugosity and fish habitats on coral reefs (Wedding *et al*., 2008) and, in combination with multi-spectral imagery, for classification of shallow subtidal seabed habitats (Chust *et al*., 2010). ALB data were used to discriminate cluster zones of massive stony coral colonies on patch reefs (Brock *et al*., 2006) and to map benthic habitats using the amplitude of the lidar bottom return (Wang and Philpot, 2007). Tulldahl and Wikström (2012) used data from the Hawkeye II to classify the seabed substratum and vegetation for a study site within the Baltic Sea, and Velasco *et al*. (2014) used Hawkeye II data to classify the seabed off the coast of Spain. The Tenix LADS (laser airborne depth sounder) Mk II lidar was used for differentiating canopy structure of macroalgae communities (*i.e.*, canopy structure classification), such as canopy forming kelp versus erect fine branching algae off the coast of Australia (Zavalas *et al*., 2014). The effects of complex bottom geometry on the shifting of the bottom peaks in the waveforms which translate into range and depth errors have been studied by Bouhdaoui *et al*. (2014) and Wang and Philpot (2007). Other studies have used data from the Joint Airborne Lidar Bathymetry Technical Center of Expertise (JALBTCX) Optech SHOALS: Arifin and Kennedy (2011) examined the evolution of large scale crescentic bars before and after hurricanes within the Gulf of Mexico. Kennedy *et al*. (2008) examined ephemeral sand waves in the response to hurricane forces in the surf zone. Reif *et al*. (2013) reviewed the use of JALBTCX ALB data to map regions of the Great Lakes from 1995–2012.

These large deep water lidar sensors have provided the background for a new generation of commercial shallow water sensors like the Leica AHAB Chiroptera, and the Reigl VQ-820-G and Optech Aquarius systems. The Chiroptera I sensor was used to map shallow lakes in Alaska (Paine *et al*., 2015). The Riegl VQ-820 and Optech Aquarius systems, and the shallow water experimental EAARL system (Nayegandhi, Brock, and Wright, 2009) rely only on a green laser for operation. Allouis *et al*. (2010) discuss methodologies to detect the water surface using near-infrared laser, Raman scattering, and a green laser. The Chiroptera series of sensors are currently the only shallow water sensors that utilize a NIR laser with a green laser to map the sea surface (Figure 1). Wang *et al*. (2015) compared a variety of waveform processing algorithms for single-wavelength lidar bathymetry systems and noted the disadvantage of the lack of a NIR channel, which results in difficulties in extracting the water surface.

Recently, the Applied Geomatics Research Group (AGRG) at the Nova Scotia Community College (NSCC) acquired a Leica AHAB Chiroptera II topobathy lidar sensor equipped with a Leica RCD30 aerial camera. In this paperthe key findings, lessons learned, and methodologies developed as a result of the first mission using the sensor, which was the first lidar topobathy survey of Maritime Canada using a Chiroptera II, are reported. Five coastal sites were surveyed from September 23 to

27, 2014, along the coast of Nova Scotia (NS) and New Brunswick (NB), Canada (Figure 2, Table 1). The coastal sites ranged from sheltered embayments that host shellfish
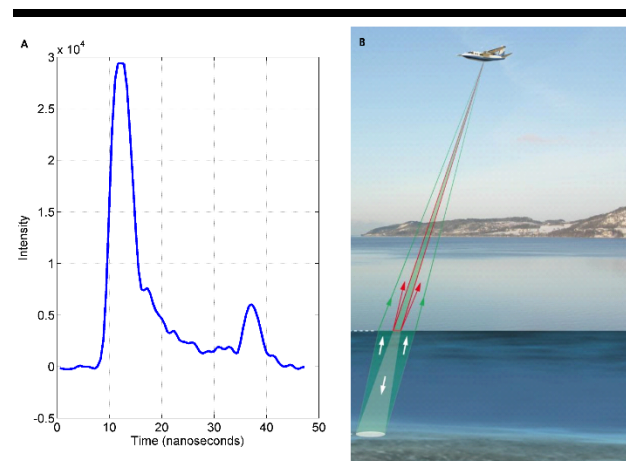

Figure 1. (A) Example of the Chiroptera II green laser waveform showing the large return from the sea surface and smaller return from the seabed. (B) Schematic of the Chiroptera II green and NIR lasers' interaction with the sea surface and seabed (adapted from Leica AHAB).
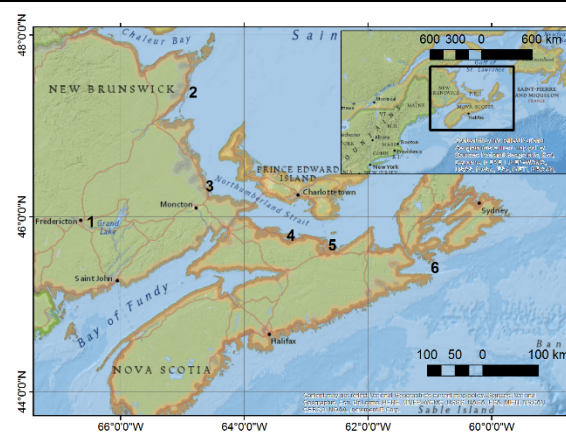
Figure 2. Study sites for the topobathy lidar coastal surveys, Maritime Canada. See site names in Table 1. Inset map at the top right shows Maritime Canada location in the North Atlantic Ocean.

aquaculture operations and bays that have potential to host aquaculture, to areas that are near the shipping lanes for petrochemical sites and are at risk of possible contamination in the event of a tanker spill.

Laser penetration is limited by water clarity, as particulate matter suspended in the water column can interrupt the laser's path to the seabed. Several of the study sites were located along the Northumberland Strait in the Gulf of St. Lawrence, where erosion of the unconsolidated red clay sediments in this region cause the coastal waters to become turbid when onshore wind

induces waves and the nearshore bottom sediment is disturbed. In section 3.1, results are presented for the Cape John, Nova Scotia, study area (Figure 2, site 4), where turbid conditions presented challenges to successful laser penetration, and measures that were taken to manage the challenge of this turbidity-prone environment are discussed, such as weather monitoring and adaptive planning.

Table 1. *Study sites in New Brunswick (NB) and Nova Scotia (NS) and main application of ALB.*

Site Number	Location	Purpose
1	Fredericton-Nashwaak River	Base of operations, calibration
2	Tabusintac, NB	Bathymetry and eelgrass mapping
3	Cocagne, NB	Bathymetry, eelgrass and shellfish aquaculture infrastructure mapping
4	Cape John, NS	Bathymetry, coastal processes, erosion, geoscience
5	Little Harbour, NS	Bathymetry, shellfish aquaculture potential
6	Isle Madame, NS	Bathymetry, shoreline physical and ecological mapping, oil spill preparedness

Initial images constructed from the amplitude of the reflected green laser return pulse indicated that the Chiroptera II sensor did not compensate for depth during the surveys. A method is presented in section 2.6 that compensates for the signal loss due to water attenuation of the green laser pulse and that adjusts the amplitude of the seabed signal to facilitate interpretation of the amplitude images of the seabed.

Several of the coastal areas contain the seagrass *Zostera marina*, or eelgrass as it is locally known, which is classified as an ecologically significant species (Fisheries and Oceans Canada (DFO), 2009) and is used by DFO as an ecosystem health indicator for the bays that host shellfish aquaculture. In section 3.4, results of using the lidar elevation data and derivatives to classify the eelgrass for the Tabusintac, NB, area (Figure 2, site 2) are presented; methodology for this approach is presented in section 2.7.

Finally, future research in the area of laser waveform analysis (section 4) is discussed. For this study, the analysis of the Chiroptera II data was completed using the discrete points derived from the waveform data in Lidar Survey Studio (LSS). However, an examination of the waveforms within LSS indicates there is additional information that may be extracted and exploited using different point classification methods. Several researchers have derived additional metrics from the waveforms to enhance seabed classification methods (Chust *et al*., 2010; Collin *et al*., 2012, 2011a, 2011b; Tulldahl and Wikström, 2012) and modeled the bias effects of seagrass on bottom elevations (Wang *et al*., 2011). This section concludes with a discussion of the concept and framework for future research initiatives for extracting more information than simply the water surface, submerged objects, and bathymetric points from the waveform using BinReader, a new software package produced by Leica AHAB.

METHODS

Sensor Specifications and Installation

The Chiroptera II topobathy lidar system is produced by Leica AHAB and exhibits many upgrades from the Chiroptera I (Airborne Hydrography AB, 2014). The Chiroptera II system incorporates a 1064 nm NIR laser for topographic returns and water surface definitions and a green 515 nm laser for bathymetric returns (Figure 1). The lasers utilize a Palmer scanner, which forms an elliptical pattern on the ground or water surface with angles of incidence of ±14° forward and back and ±20° to the sides of nadir along the flight track. This enables more returns from a single target than systems that utilize a linear scanning pattern, thus reducing shadow effects and increasing the number of points on vertical faces such as cliffs along the coast. The elliptical scan pattern results in the target being surveyed twice from different angles a few seconds apart; therefore, it is less sensitive to ocean wave interaction where the air bubbles of a breaking wave will attenuate the green laser pulse and prevent penetration to the seabed. The beam divergence of the topo laser is 0.5 milliradians (mrad) and is 3 mrad for the bathy laser. The topo laser has a pulse repetition frequency up to 500 kHz, and the bathy laser has a pulse repetition frequency 35 kHz. The point density and accuracy specifications assume a flight altitude of 400 m above ground level (AGL) with a flight speed of 60m/s. The maximum operational altitudes are 600 m AGL for the bathy laser and 1,600 m AGL for the topo laser. The point density is 1.5 pts/m^2 for the bathy laser and greater than 12 pts/m^2 for the topo laser at 400 m AGL. The bathymetric accuracy of the bathy lidar is within 0.15 m at 2 standard deviations (95% confidence interval), and the topo laser has a ranging/vertical accuracy of 0.02 m at 1 standard deviation (68% confidence interval) and a horizontal accuracy of 0.2 m at 1 standard deviation, not including GPS-IMU (inertial measurement unit) error. The system is equipped with a standard 5 MPIX RGB camera capable of exposures at 1 frame per second for quality assurance purposes and is linked to the timing of the laser points and can be queried within LSS. The Leica RCD30 camera collects co-aligned RGB+NIR motion-compensated photographs, which can be orthorectified and mosaicked into a single image in post-processing or analyzed frame by frame for maximum information extraction. The RCD30 is a 60 MPIX camera capable of exposures at 0.8 frames per second with a distortion-free lens with a focal length of 53 mm and produces images 6,732 by 9,000 pixels in the across- and along-track direction, respectively. The across-track field of view of the camera is 43.8°, which is slightly wider than the across-track lidar field of view, which is 40°. At 400 m altitude, the RCD30 produces imagery with a 5-cm pixel resolution.

The depth penetration of the bathy laser is limited by water clarity. Secchi depth is a measurement of water clarity wherein a deeper Secchi depth indicates clearer, or less turbid, water and a shallow Secchi depth is an indication of less clear, or more turbid, water. The Chiroptera II sensor is stated to have a depth penetration of 1.5 times the Secchi Depth, where the Secchi Depth is approximately equal to 1.6/Kd, where Kd is the diffuse attenuation coefficient (AHAB, personal communication). The sensor specifications state that for a bottom reflectance of 15% with 532 nm light and Kd ranging from 0.15 to 0.25, the depth

_____

penetration expected is 15 m and 9 m, respectively. These values provide upper limits for the range of depth penetrations that might be expected in the coastal environments being studied.

The sensor was installed in a Beechcraft A90 King Air aircraft on September 22, 2014, and calibration flights were conducted over Fredericton, NB, at altitudes of 400 m and 1,000 m on September 23 (Figure 2, site 1). The calibration survey area consisted of several types of building roof styles with many flat planes sloping in different directions. These roof planes are used in the automatic matching procedures during the calibration process to calculate the laser and GPS-IMU alignment. The calibration was deemed a success when lidar topo points and bathy laser points obtained during flight lines in opposite, parallel, and perpendicular directions agreed to within the manufacturer's specifications (*e.g.*, within 2 cm in the vertical and within 20 cm in the horizontal, (Airborne Hydrography AB, 2014)) and when 95% of lidar points agreed with survey grade GPS at several altitudes to within 10 cm in the vertical on flat surfaces.

Lidar Survey Details

Meteorological conditions during topobathy lidar surveys are an important factor in successful data collection. As the depth of laser penetration is limited by water clarity, windy weather that stirs up sediment in the seawater can prevent good bottom returns. Rain or foggy weather is not suitable for lidar collection, and the reflection of the sun off the water must also be factored in for aerial photography acquisition. In order to survey during optimal conditions, a combination of publicly available weather data and data from weather stations installed by AGRG where public stations were too far from the study sites was used. These data were used to check the weather conditions remotely and to use in post-processing to enhance operational efficiency with turbidity management and optimal survey conditions. In addition to examining the weather data as part of the turbidity management process during survey planning, individuals at marinas near the study sites were contacted for first-hand accounts of local water clarity conditions.

The coastal bathymetric surveys were acquired at an altitude of 400 m with 30% overlap between flight lines at a flying speed of 55 m/s, resulting in a swath 291 m wide with a bathy lidar spot spacing of 1.56 m forward lateral spacing and 0.78 m front to back scan spacing as a result of the forward progress of the aircraft, resulting in an average point density of 1.65 points/m^2. The green laser spot diameter on the water surface is approximately 1.2 m at 400 m altitude, and the topo laser is 0.2 m. In general, flight lines were flown parallel to the coastline with an additional line planned perpendicular to the coastline that intersects the coast parallel lines. This perpendicular line was ideally selected in a location with homogeneous seabed cover material and was planned to be used to compensate for the reflected green laser amplitude signal for depth.

This paper focuses on the results from Tabusintac, NB, Cape John, NS, and Little Harbour, NS (Figure 2, sites 2, 4, and 5), which were surveyed on September 25 and 26. In the week preceding the surveys, the weather data indicated a significant storm event occurred in the Northumberland Strait area with a drop in barometric pressure and associated wind speeds exceeding 40 km/hr from the northwest and rainfall from

September 18–22. Following the storm, a high pressure system moved into the region providing clear skies; however, the winds persisted between 20 and 40 km/hr into the next week.

The survey of Little Harbour, NS, was conducted with good penetration observed during the flight on September 25, 2014, in the late morning amid small white caps but good water clarity (Figure 2, site 5). In Cape John, however, even a moderate wind can stir up the fine sediment in the area, and the wind had been blowing at 20–50 km/hr from the southeast for 12 hours. An attempt was made to survey this area despite the wind, and some good returns were obtained on the north side of the study area, but the survey was aborted due to poor bathymetric returns observed during the flight for the south side of Cape John as a result of turbid water conditions. Tabusintac, NB, was surveyed on September 26 starting near noon (Figure 2, site 2) in low wind conditions; good laser penetration was observed during the flight. The wind began to die down at Cape John in the early morning on September 26, and by late afternoon of that day conditions were suitable to complete the survey there after Tabusintac was completed. The wind data for Cape John and a more detailed discussion of the management of turbidity issues encountered there are presented in section 3.2.

In situ Sampling

Ground truth data is another important aspect of TBL data collection, as noted by Shachak *et al.* (2013), especially since this was the first survey in the region with the Chiroptera II system. For most sites a Leica GS14 GPS system was used to set up a base station for the aircraft over a High Precision Network (HPN) monument or equivalent, and in some cases a temporary marker was established ahead of time and rapid static GPS coordinates were obtained and referenced to the HPN network. In some cases, ground crews were not able to establish a local GPS base station and the CANSEL^{TM} virtual reference network was used as a reference station for the aircraft. The local GPS data from the base and from the virtual network were required for the aircraft in order to obtain high accuracy positional data.

In cases where a local base station was established, RTK GPS checkpoints were collected along hard flat surfaces to validate the elevations obtained with the topo laser. Several methods of depth measurements were employed during boat-based ground truthing to compare to the bathy laser, including a lead ball on a graduated rope and several different brands of sonar and echosounder. A single beam consumer grade echosounder with a code-based GPS (horizontal accuracy ~5 m) was used to survey the depths within most of the study sites, and various point observations were made to sample the water column and bottom conditions. The point observation method consisted of taking a handheld GPS waypoint (horizontal accuracy ~2–4 m), taking a Secchi disk measurement (a depth measurement using a lead ball) and dropping a 1 m by 1 m quadrat over the side equipped with two GoPro^{TM} underwater cameras to take still photographs of the seabed at 5-second intervals with 4,000 x 3,000 pixel frame resolution. One camera was mounted downward-facing to get a plan-view photo and the other mounted side-facing to get a cross-section view (Figure 3). A vertical arm was constructed to be in the field of view of the side-mounted camera with graduated marks every 20 cm to estimate the height of the submerged vegetation. The photographs were examined

manually in post-processing and assigned a value of eelgrass presence or absence. Bottom type information is useful for research related to returning laser amplitude and for submerged vegetation mapping validation (Shachak *et al*., 2013). Scientists from DFO Gulf Region provided additional eelgrass presence/absence ground truth data, underwater light measurements, and bottom descriptions for several sites, including Tabusintac, Little Harbour, and Cocagne. Stantec Consulting provided eelgrass presence/absence ground truth data for Tabusintac. Both of these datasets were georeferenced using code-based GPS.
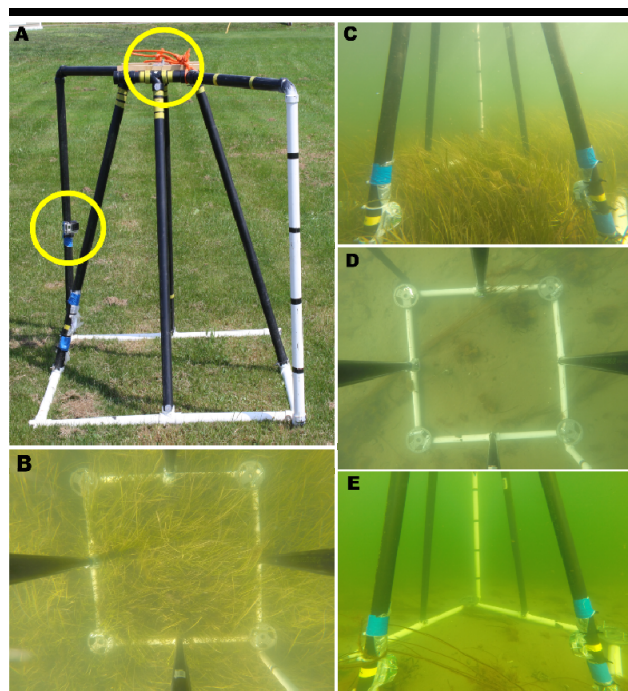

Figure 3. Example of in situ quadrat and seabed photos. (A) 1 m by 1 m quadrat frame for seabed photos showing the location of the vertical and side view camera in yellow circles. (B) Example of vertical photo of the quadrat with 100% eelgrass, (C) example of side view photo of the quadrat with 100% eelgrass, (D) example of vertical photo of the quadrat with 90% sand, and (E) example of side view photo of the quadrat with 90% sand.

Lidar and Air Photo Processing

LSS was used to process the aircraft trajectory using the GPS base station data, and to georeference and link the navigation data to the laser returns. The lidar returns from both the topo and the bathy lasers were then classified as discrete land, water surface, or bathymetry points. The LSS software automatically interpolates the water surface points to produce a continuous modeled water surface regardless of the original varying lidar point density. Bathymetry points were classified using threshold parameters related to the green laser waveform, which are set within LSS; additionally, a pre-release of a new murky water algorithm was made available by AHAB, which improved the

number of candidate bathymetric points in the classification process. The classified point data were examined in LSS using a variety of attributes (flight line, elevation, intensity) and the 5 MPIX quality control air photos for quality control (Figure 4). The waveform accessible in LSS shows the "return window" portion of the waveform that is offset from the transmitted pulse, "T0" (Figure 4A). The x-axis in LSS represents the sample interval from the return window offset, which can be related to time: 10 samples = 5.5 nanoseconds. The y-axis represents the return green laser intensity that is unitless and dependent on the optical receiver and digitizer.

The classified points can be exported in LAS 1.2 or 1.4 and further refined and filtered to reduce noise. Classification codes for bathymetric points (LAS 1.4) were used and the data were exported to LAS 1.2 in order to facilitate further processing in other software. The LAS files were read into TerraScan^{TM} with the laser returns grouped by laser type so they could be easily separated, analyzed, and further refined. Macros were written to improve the separation of bathymetric points and noise and attempt to classify submerged vegetation. There is no specific class code for submerged aquatic vegetation defined in LAS 1.4 at this time; the techniques developed for classifying eelgrass are further discussed in section 2.7.

Because of the differences in the lidar footprint between the topo and bathy lasers, the bathy point returns would be used to represent the water surface and bathymetry points, and the topo points would be used to represent targets on the land. The refined classified LAS files were read into ArcGIS^{TM}, and a variety of raster surfaces at a 2-m spatial sampling interval were produced. Several data products were derived from the lidar point cloud including the Digital Surface Model (DSM) and the Digital Elevation Model (DEM), which are based on topographic and bathymetric elevations. The DSM incorporates valid lidar returns from vegetation, buildings, and ground and bathymetry returns, and DEM incorporates ground returns above and below the water line. The elevation of the lidar point cloud is relative to the WGS84 ellipsoid since the points are geolocated based on the GPS aircraft trajectory. However, once the surface models (DSM and DEM) were constructed using different combinations of the point class elevations, these data were converted to orthometric heights and are now relative to the Canadian Geodetic Vertical Datum of 1928 (CGVD28). The geoid-ellipsoid separation model, HT2, from Natural Resources Canada was used to apply this conversion to the surface models.

The bore site for the RCD30 60 MPIX camera was computed and the imagery was processed using the aircraft trajectory and direct georeferencing. The low altitude and high resolution of the imagery required that the lidar data be processed first to produce bare-earth DEMs that were used in the orthorectification process. The aircraft trajectory is linked to the laser shots and photo events by GPS-based time tags and was used to define the Exterior Orientation (EO) for each of the RCD30 aerial photos that were acquired. The EO and lidar DEM were coupled with the aerial photos to produce digital orthophotos using Erdas Imagine^{TM} software. The orthophotos were imported into ArcGIS^{TM} and various mosaic options were tested to determine the best solution to provide the most detail of the submerged features. The visibility of submerged features
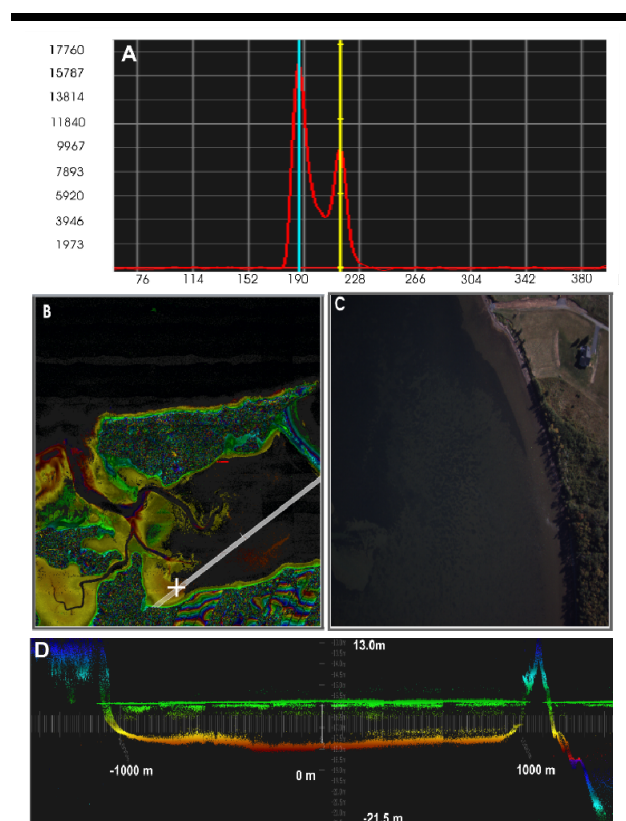
Figure 4. Example of screen grab from LSS for the Little Harbour, NS, site. (A) Shows a waveform associated with a lidar return denoted by the + along the cross-section white line in (B). The waveform x-axis is a time sample, y-axis is intensity, with the water surface (blue line) and seabed (yellow line) peak defined with vertical lines. (B) Plan view of lidar data colored by elevation with cross-section (white bar). (C) 5 MPIX airphoto associated with the lidar return + in (B). (D) Cross-section of bathy lidar points colored by elevation for the white line in (C), x-axis is distance and y-axis is elevation relative to WGS84.

was mostly dependent on the presence or absence of sunglint caused by the reflection of light onto the camera head. In the majority of cases, glint was constricted to the corner portion of the photos and was removed using a preferential ordering technique that ensured these areas were overwritten with overlapping photos that contained no glint. In a small number of cases, glint was present throughout the photos due to the declination of the sun and wave action. Glint was removed from these problematic photos using pixel statistics from overlapping photos to identify and reject pixels with abnormally high spectral responses in the mosaicking process, *i.e.* taking the pixel with the lowest value. The use of these combined techniques resulted in a mosaic image that was virtually free of sunglint.

Lidar Validation

Various GPS checkpoints were collected to compare to the lidar points and surface models to ensure the vertical accuracy of the data was sufficient. The GPS elevations were converted from ellipsoidal height to orthometric heights using HT2. Those GPS points that represent the bare ground were then overlaid with the lidar DEM, and the raster cell value was appended to the point file. Differences in elevation between the GPS points and the lidar-derived DEM were computed and summary statistics calculated.

Bathymetric lidar validation was achieved by comparing boat-based depth measurements taken synchronously with the lidar survey. The precision of the code-based GPS built into the consumer grade depth sounder was not sufficient to validate the lidar bathymetry data (~5 m). Additionally, the sounder had no capability to fine-tune salinity values; it could only be set to salt water or freshwater, and surveys were often conducted in estuarine environments. Since the precision of the handheld GPS used to mark waypoints was slightly better (2–4 m) than the sounder and presented no concerns related to speed of sound calculations, the manual depth measurements taken with the lead ball coincident with the lidar survey were used to validate the bathy lidar depths. The manual depth measurements were subtracted from the water surface derived from the lidar data and compared with the bathymetric DEM using a similar technique as described for the topo lidar validation.

Depth Normalization of Green Laser Amplitude

The amplitude of the returning signal from the bathy laser provides a means of visualizing the seabed cover (Figure 5A). The amplitude of the returning signal is influenced by several factors, including water depth and clarity, the local angle of incidence with the target, the natural reflectivity of the target material, and the voltage or gain of the transmitted lidar pulse. The raw amplitude data are difficult to interpret because of variances as a result of signal loss due to the attenuation of the laser pulse through the water column at different scan angles. Gridding the amplitude value from the bathy laser results in an image with a wide range of values that do not compensate for depth and have significant differences for the same target depending on the local angle of incidence from flight line to flight line. As a result, these data are not usable as is for quantitative analysis and are difficult to interpret for qualitative analysis.

The raw amplitude of the flight lines displayed significant variance in overlap regions between lines that were flown in opposite directions. The flight plan was such that even and odd numbered lines were flown in opposite directions. In order to minimize the inter-flight line variance, the raw amplitude values for even and odd flight lines were rasterized to a 2-m grid cell using the maximum amplitude value for each grid cell from the green laser points. This resulted in two rasters that represented the amplitude for the even and odd numbered lines flown in opposite directions. These rasters were overlaid and the difference calculated for the overlap region. The resultant difference raster was smoothed with a low pass filter and re-interpolated using a spline function across the overlapping boundary. The resultant smoothed difference raster was then applied through addition and subtraction to the even and odd amplitude images, respectively, for the overlap regions. The result was to smooth and blend the amplitude values across the flight lines flown in opposite directions. These final even and

odd flight line adjusted amplitude rasters were then used to construct a mosaic where the flight line direction differences were minimized (Figure 5A).
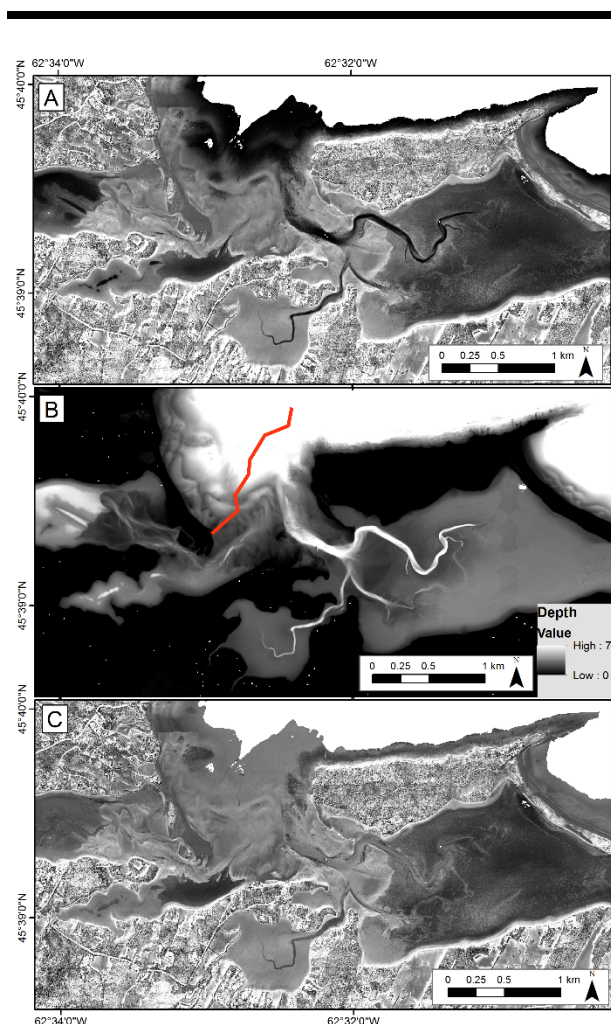

Figure 5. (A) Line-matched amplitude of the green laser for Little Harbour. (B) Depth map with sample locations (red line). (C) Depth-normalized amplitude image.

One flight line was flown perpendicular to the coastline for each site with the intent of sampling the return amplitude of the green laser for a homogeneous seabed cover at different depths to empirically correct the amplitude for depth attenuation. Unfortunately, homogeneous samples were difficult to obtain within these flight lines, so this line was not always used to normalize the amplitude of the green laser. Instead, a sample of line-matched amplitude values were selected wherever a common cover type (*e.g.*, sand or eelgrass) could be located over a range of depths (Figure 5B). These data were used to

establish a relationship between depth and the logarithm of the amplitude value. The inverse of this relationship was used with the depth map to adjust the amplitude data so that they could be interpreted without the bias of depth. A depth-normalized amplitude image was created using this technique that can be more consistently interpreted for the seabed cover material (Figure 5C). Note that this analysis considers only bathymetric lidar values and ignores any topographic elevation points.

Eelgrass Mapping

The derivation of eelgrass distribution from the lidar data is an active area of research for the authors. Although the pulse width of the bathy laser is very small (1.9 ns) and thus is capable of separating targets that are very close in range, such as the water surface and the seabed, it is challenging to map the seabed where dense eelgrass exists. The approach developed here for classifying eelgrass was designed to exploit the seabed roughness signals derived from the bathymetric lidar points. The classified bathymetry points were gridded to 2-m cell resolution taking the maximum elevation of the lidar bathymetry points within each grid cell. From this bathymetry grid, slope and aspect grids were constructed. A statistical function using a 3x3 cell window was executed on the slope and aspect to calculate the standard deviation of these values within the 3x3 kernel. The following equation describes the process of identifying an eelgrass detection index, *EDI*:

$$EDI = \sigma(\theta) * \sigma(\sin(\propto)) * \frac{\sqrt{d}}{(d+1)^{\frac{d}{F}}} \qquad (1)$$

where $\sigma(\theta)$ is a raster of the 3x3 standard deviation (σ) of slope (θ) of the DEM, $\sigma(\sin(\propto))$ is the raster of the localized (3x3) standard deviation of the sin of the aspect, $\propto$, of the DEM, d is the raster of water depth collected at the time of flight constructed by subtracting the bathymetric DEM from the water surface DEM, and F is a factor which represents the most probable depth of eelgrass. The standard deviation of slope and aspect was combined through multiplication and scaled by depth through dividing the product by the depth grid. This produced a grid that represents a range of values based on seabed roughness, which is acting as a proxy for eelgrass distribution. Because σ(slope) is high for areas of high bed roughness and uniform terrain slope, while σ(sin(Aspect)) is high in areas of varying degrees of bed roughness, yet low in areas of uniform terrain slope, the signals of σ(slope) and σ(sin(Aspect)) can be multiplied to represent the amount of apparent bed roughness. Areas of high bed roughness correlated highly to the distribution of eelgrass as observed from aerial photographs. However, due to the accumulated signal loss of laser light, the precision of bottom surface detection of bathymetric lidar decreased with depth, resulting in an increase of the apparent bed roughness detected in deeper areas. Additionally, eelgrass distribution is light limited and is thus closely bound to a shallow range of water depths. Therefore, the final term of Equation 1 is multiplied by the apparent roughness to account for the depth distribution of eelgrass. It uses a constant, F, to represent the most probable depth of eelgrass. F ranges between 1 and 3 m

_____

were tested and a final value of 1.5 m was chosen by comparing resulting eelgrass maps to underwater and aerial imagery. The resulting eelgrass detection index can be converted into eelgrass distribution maps showing eelgrass presence/absence by applying empirically determined thresholds to the eelgrass detection index. The thresholds were chosen by comparing the resulting maps to ground truth data.

RESULTS

Lidar Validation

GPS checkpoints were compared to the topo lidar-derived surfaces for Cape John, Little Harbour, and Tabusintac. The differences between the GPS elevation and the DEMs, *DZ*, are summarized in Table 2. The DEMs tended to slightly over-predict the elevations compared to the GPS points, and mean differences and standard deviations were 5 cm or less. In the case of Tabusintac, NB, and Cape John, NS, GPS points were collected along the wharf deck and parking lot and used for the validation. At Little Harbour, NS, the GPS antenna was mounted on a vehicle and GPS points were collected along the roads across the study area as well as from a pole at the parking lot and dune pathway.

Table 2. *Comparison of GPS checkpoints and topo lidar DEM.*

Location	Mean DZ (GPS-DEM) (m)	DZ standard deviation (m)	Number of checkpoints
Cape John	-0.02	0.04	13
Little Harbour	-0.05	0.04	3606
Tabusintac	-0.05	0.02	37

The validation of the depths was accomplished for Tabusintac using manual depth measurements and extracting the water surface elevation from the lidar. The depth was then subtracted from the lidar water surface and compared to the lidar elevation model. The horizontal positional accuracy of the depth measurements was based on a code GPS solution, which has 2–4 m of uncertainty. There was a mean difference between the 18 computed seabed elevation points and the lidar seabed elevation of –0.07 m, but the standard deviation was high (0.26 m). The largest errors appeared to be two points collected near the channel slope and may have been related to the positional accuracy of the ground truth data as well as the uncertainty introduced by a sloping surface on the lidar waveform. With these points removed, the mean becomes 0.004 m and the standard deviation reduces to 0.12 m.

Turbidity Management

Turbidity management is an important aspect of operational success during a TBL campaign. The ability to survey alternate sites with different coastline orientations and exposure allows for higher probability of a successful TBL data collection considering the environmental conditions. Strong winds preceding and during the planned lidar survey of the Northumberland Strait affected water clarity at some study sites by stirring up sediment into the water column. The water clarity at Cape John was most severely affected by strong winds

blowing from the southwest between September 22 and 24 at speeds between 20 and 50 km/hr (Figure 6B). By late September 24, the wind had peaked and shifted to be from the north, then decreased on September 25 back to less than 20 km/hr from the south.

A successful TBL survey was conducted at Little Harbour, NS, on September 25, and an attempt was made at Cape John on the same day. Although the wind decreased at Cape John on September 24, it was not for a sufficient length of time to allow the sediment to settle in John Bay on the south side of Cape John prior to the flight on September 25 (Figure 6B). As can be seen in the orthophoto on September 25, the water on the south side of Cape John is highly turbid and waves are present compared to relatively clear water and no waves on the north side. Continued low wind speeds from the south through the evening of September 25 and through the day on September 26 allowed the sediment to settle in John Bay on the south side of Cape John peninsula. When surveyed late in the day, the orthophotos show improved water clarity in the south with sand bars visible through the water and similar conditions in the north as were present on September 25 (Figure 6C). The difference of one day without significant wind and wave action allowed the suspended sediment to settle and reduce the turbidity on the south side of Cape John. The test line highlighted with the red ellipse in Figure 6 was flown on September 25 and 26 to compare water clarity and lidar penetration conditions at Cape John as seen on the orthophoto and lidar cross-sections (Figure 6, 7).

The lidar data were processed for this test line from both surveys (September 25 and 26) and analyzed for surface and depth penetration (Figure 7). The southerly wind generated onshore waves for John Bay, which caused increased turbidity compared to the north side where waves were minimal on September 25, resulting in no depth penetration of the laser on the south side but equal penetration on the north side for both days (Figure 7A). The surface waves can be observed from the southern lidar cross-section on September 25 (green) compared to the calm water on September 26 (yellow) (Figure 7A).

On September 26, the sediment had settled to the point of allowing the bathy laser to penetrate to a depth of 5 m on both the north and south side of Cape John (Figure 7). Methods to improve operational awareness for turbidity management are a continuing area of research at AGRG. These efforts include building up a time-series from coastal weather stations and in situ sensors measuring light penetration and turbidity.

Lidar Surface Models

In order to easily interpret the lidar surface models, color shaded relief (CSR) models were constructed from the DSM and DEM for the study sites (Figure 8A). The CSR maps were colorized to take advantage of Chroma-stereoscopy where the lower elevations are color-coded from the short wavelength blue to higher elevations at longer wavelength red. When the maps are viewed with ChromaDepth™ glasses, it appears in 3D. The depth-normalized amplitude image was integrated into the colour shaded relief DEM for the Little Harbour study site to facilitate geomorphic and benthic habitat interpretation (Figure 8B). Underwater and aerial imagery were used to aid in the
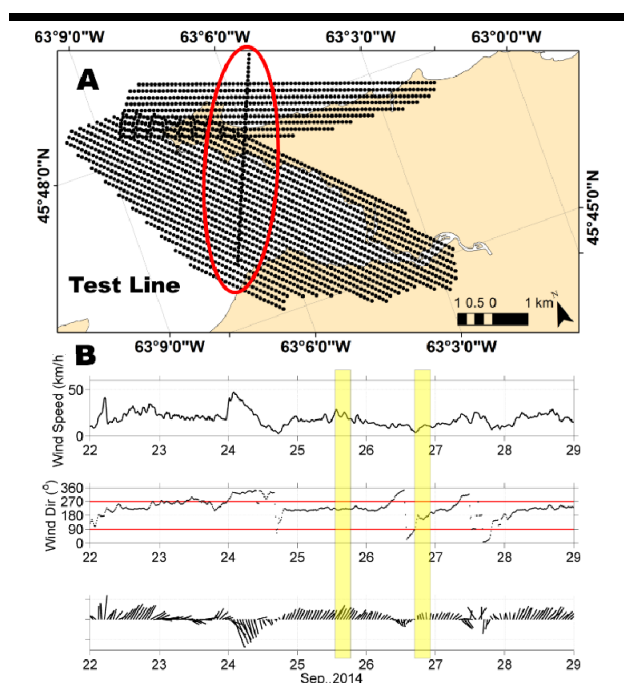
Figure 6. Comparison of water clarity at Cape John, NS. (A) Cape John peninsula with the planned flight lines including the test line (red ellipse). (B) Weather data with wind speed (top), wind direction (middle), and quiver plot (lower) for Cape John with survey dates highlighted in yellow bars. (C) The test survey line orthophoto on September 25 on the left and September 26 on the right showing significant turbidity on the south side (lower body of water, red lines) of Cape John compared to the north side (upper body of water, yellow lines).
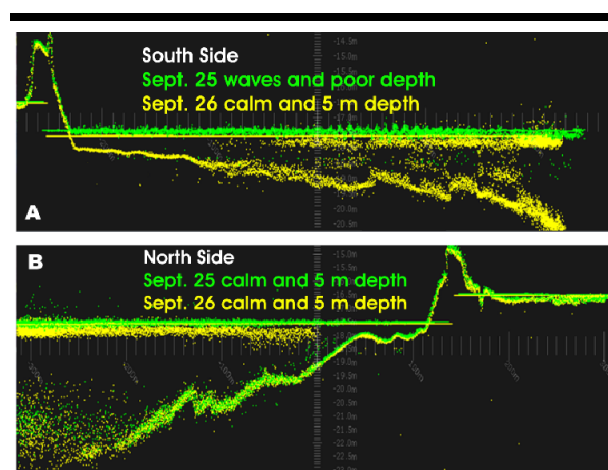

Figure 7. (A) Lidar cross-section (red line on Fig. 6 orthophotos) of the south side of Cape John, NS, with no seabed returns on Septemebr 25 (green points) and good returns on September 26 (yellow points). (B) Lidar cross-section (yellow line on left orthophotos) of the north side, which did have seabed returns during both surveys on September 25 and 26 (green and yellow points, respectively).

interpretation of the submerged bathy amplitude image in combination with the orthophotos and the texture of the shaded relief map and found that the darker tones are indicative of the occurrence of eelgrass, while the smooth flat and bright tones can be interpreted as sand or sand ripples in the channel.

Eelgrass Distribution Maps

An eelgrass map was derived from the lidar elevation parameters only for Tabusintac Bay. The methodology exploited the variability in the elevation of the lidar returns where a rougher bottom corresponded to eelgrass compared to a smooth sandy bottom. The map was constructed by combining a variety of lidar elevation derivatives including depth and the variability of slope and aspect. This produced a map with a range of values representing different levels or likelihood of eelgrass occurrence, which was then simplified into a presence-absence map. This map was compared to the boat-based ground truth collected by researchers from AGRG, DFO, and Stantec Consulting where the presence or absence of eelgrass has been determined by underwater photographs. Of the 69 ground truth points, 55 matched the lidar-derived map in terms of presence or absence of eelgrass, indicating an 80% agreement (Figure 9). Research into utilizing the normalized amplitude and exploring the waveforms associated with eelgrass is planned for future studies.

DISCUSSION

Understanding the thresholds of wind direction and speed on water clarity conditions to allow for a successful TBL survey could improve the operational efficiency and awareness and provide major cost savings to lidar operators through better turbidity management processes and knowledge of the survey sites. In this study, weather station data proximal to the study sites were examined with respect to the orientation of the
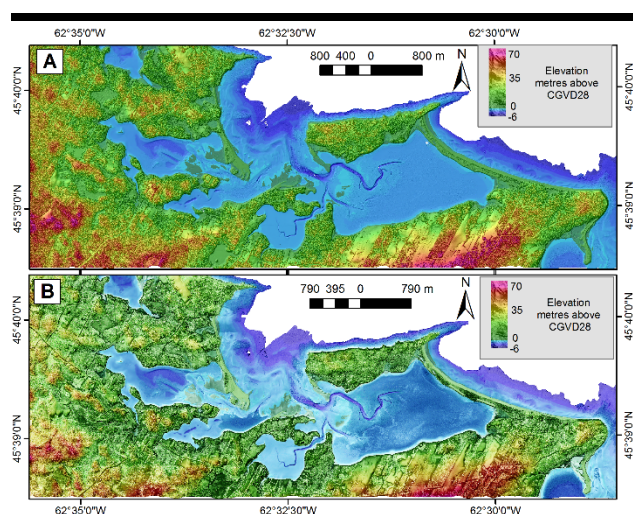
Figure 8. (A) Map of color shaded relief of the DSM at Little Harbour, NS. (B) Map of the color shaded relief of the DSM integrated with the depth-normalized amplitude from the green laser.
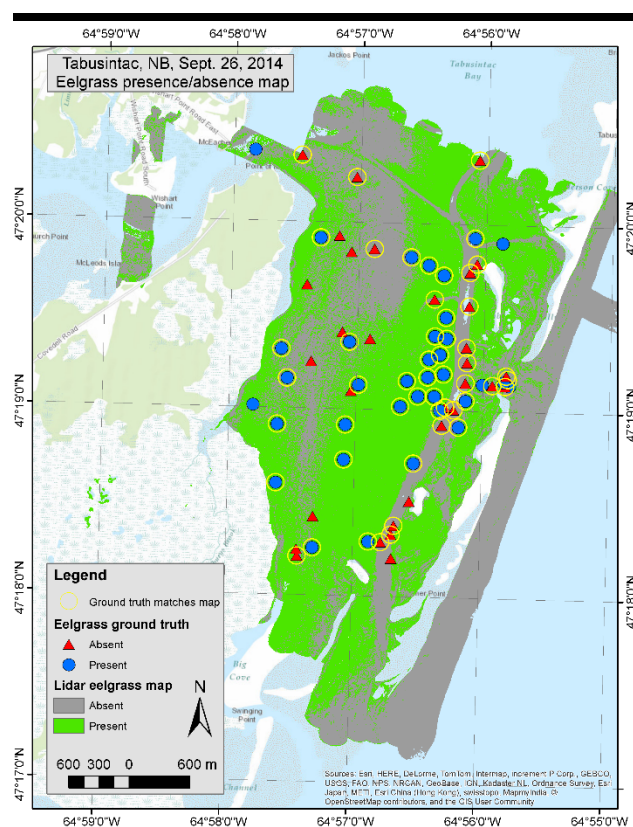

Figure 9. Eelgrass map for Tabusintac, NB, derived from lidar elevation parameters. Ground truth indicates eelgrass presence (blue dots) and absence (red triangles) match the map (yellow circles).

coastline and study site to determine the exposure of the coastline to onshore wind and waves. If onshore waves occurred, then there was a high probability that turbidity levels were also high and that the likelihood of a successful TBL survey was low; therefore, another candidate site was evaluated and surveyed if conditions were acceptable. The data from Cape John demonstrate the potential for high turbidity levels to occur locally within the water column and limit depth penetration of ALB sensors during onshore wind events. Similarly, that area also shows that over a single day of reduced wind speeds the sediment can settle out and the water clarity can improve to achieve a successful TBL survey. Future research plans involve continuing to build the time series of weather conditions, mainly wind speed, direction, and rainfall, and to deploy more in situ water clarity monitoring systems such as turbidity and light sensors. It is noted that during the surveys the maximum depth penetration was 6 m, short of the 9–15 m that the sensor is capable of. Future work in relating wind and light levels will also include more research into Kd values for Maritime coastlines to enable the fine-tuning of depth penetration expectations and turbidity management methods further.

Wang and Philpot (2007) reviewed the various factors affecting the amplitude of the reflected green laser pulse. The authors corrected the amplitude for the bottom returns for pulse stretching due to bottom slope using a simple radiative transfer model where the exponential attenuation of the reflected signal through the water column was accounted for. Similarly, Bouhdaoui *et al.* (2014) modeled the bottom geometry effects on peak time shifting of the lidar waveforms. In this study, the amplitude of the reflected pulse was empirically sampled across multiple depths for a common seabed cover type and the values were fitted to an exponential function to normalize the amplitude of the pulse. Although research has concentrated on validating the topo lidar using survey grade GPS checkpoints, it

is observed that the manually surveyed bathymetric checkpoints agree with those of the lidar bathymetry within the sensor's 15-cm accuracy specifications, except along the channel slopes in Tabusintac Bay. Although the horizontal positional accuracy of the ground reference data is only based on code GPS solutions, the increased error near the channel could be a result of the pulse stretching effect described by Wang and Philpot (2007) and modeled by Bouhdaoui *et al.* (2014), since these are the only areas that exceed the 15-cm difference in elevation.

Wang and Philpot (2007) also describe variability within flight lines as a result of the effect of surface waves on the bottom reflectivity. Although small surface waves were present at most sites, significant effects from waves were not observed, but effects at the overlap between flight lines that are attributed to variations of the local angle of incidence of the laser pulse and the seabed surface were observed. This effect was also highlighted by Wang and Philpot (2007), who describe the between-flight line variation and the changes in the viewing orientation. This is consistent with observations of the differences in the amplitude of the same seabed cover between flight lines flown in opposite directions. Image processing methods were used to compensate for the variance of the amplitude in the gridded images between flight lines. Although

the normalized amplitude image was not used for quantitative mapping of eelgrass, Wang and Philpot's suggestions of how to improve on a bottom map by using the lidar waveforms is sensible and forms an integral part of future research objectives in this area.

Wang *et al.* (2011) modeled the effects of seagrass-induced error on bathymetry with ALB and found that it caused a bias that is proportional to the effective leaf-area index using a SHOALS 1000 specification of a 7 ns pulse width for the simulations with a beam divergence of 5 mrad. Although limited bathymetric checkpoints existed, this bias was not observed. In this study, the eelgrass was often at an angle because of the tidal current during the survey, which would lessen the effect. Another difference is that the Chiroptera II has a shorter transmitted pulse length of 4 ns compared to the simulated SHOALS 7 ns pulse length, which may allow for targets closer together, such as eelgrass and the seabed, to be resolved.

Several authors have described using ALB depth derivative such as slope, deviation of depth, and rugosity (Collin *et al.*, 2011b; Wedding *et al.*, 2008; Zavalas *et al.*, 2014), and others have used depth derivatives in combination with amplitude or bottom reflectance (Chust *et al.*, 2010; Collin *et al.*, 2012; Velasco *et al.*, 2014; Wang and Philpot, 2007). Others have extracted different metrics from the bottom waveform and used them in classification (Collin *et al.*, 2011a; Tulldahl and Wikström, 2012). Chust *et al.* (2010) used Hawkeye II data and found that the topographic variables alone gave them low accuracy for classifying 15 intertidal and submerged habitats at 52.4% including the bottom reflectance improved it to 65.4%. The authors state that reflectance did not appear to be particularly useful for classification, and when the lidar was combined with multispectral imagery the resultant accuracy improved to over 80% with 22 classes. Collin *et al.* (2012) normalized bottom reflectance data by applying a logarithmic function and used it in combination with secondary derivative from the bathymetry DEM to classify brown algae and sediment at the 74% and 93% accuracy level and were able to map the canopy structure of kelp beds. Tulldahl and Wikström (2012) compared the results of seabed substratum and vegetation mapping from depth-derived variables alone and with the additional of waveform variables. The depth derivatives were slope and depth deviation, and the two waveform variables were bottom pulse width and pulse area. The authors utilized the maximum likelihood classifier for the classification of these inputs into three classes (hard substrate, soft substrate with high vegetation, and soft substrate with low vegetation). The results indicate that the inclusion of the waveform variables improved the classification accuracy to 86% when compared to independent data. The authors also found that the pulse width measurement gave the best results when calculated at the 20% level of the peak area, slightly better than at the 50% level of the peak area and significantly better than at the 80% level. In this study, only depth-derived variables were used where essentially rugosity was being mapped and usedas an indicator of eelgrass. The results indicate an 80% agreement when compared to independent data.

The BinReader software product by Leica AHAB allows one to read and manipulate raw waveform data from the Chiroptera II. The software has a plugin architecture that can be used to convert and manipulate the raw data such as applying algorithms and saving results to LSS files. Algorithms can be written to derive metrics of the waveforms in C++, and these metrics can be written out to a file with an associated geographic location and an associated metric (*i.e.,* area under the curve of the sea bed waveform). The plugins are written in C++ and result in dynamic link libraries (dll) that extend the functionality of the LSS Bin Reader software. An example of two waveforms that represent a sandy bottom compared to a vegetated bottom are presented (Figure 10). The waveform associated with the vegetation has a small peak prior to the strong bottom return that was not detected by the automatic point classifying in LSS (Figure 10B, "ND"). Presently, the method to classify the waveforms into discrete points within LSS is problematic for detecting such subtle features, which is interpreted to be vegetation as it exhibits a strong signal between the water surface (Figure 10B, "WS") and near the bottom (Figure 10B, "B"). Custom algorithms developed in BinReader to extract this subtle information from the waveform allow for more advanced mapping and metrics to be derived from the lidar data.
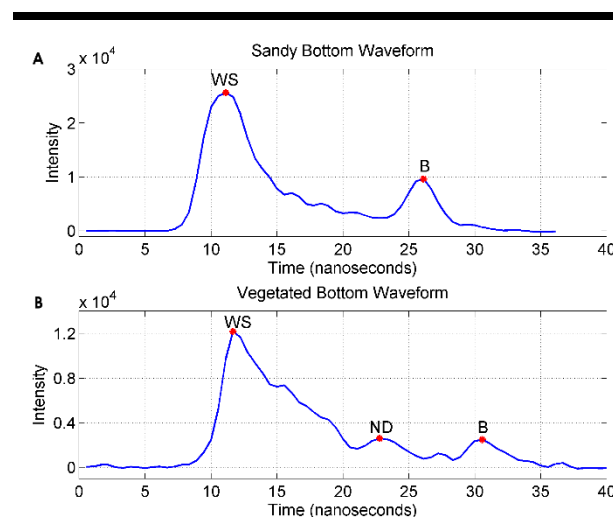

Figure 10. Example waveforms from the Chiroptera II extracted using the BinReader software. (A) Waveform from a sandy bottom return. (B) Waveform from a sandy bottom with submerged aquatic vegetation return. WS – water surface position, B – bathymetric point position, ND – not detected point.

At this point, BinReader is being used to examine and export waveforms, and the research team plans to use the software to derive variables such as pulse width and pulse area similarly to Tulldahl and Wikström (2012) to see if accuracy can be extended, and to derive other information such as density of eelgrass. The amplitude normalization process will be refined in the future following the steps outlined by Wang and Philpot (2007) and test if including that will improve the classification. Several authors are beginning to use regression tree approaches to classification like Random Forest or QUEST (Collin *et al.*, 2011a; Zavalas *et al.*, 2014) that also appear to offer certain advantages over traditional pattern recognition approaches like

___

maximum likelihood or unsupervised approaches like K-means (Chust *et al.*, 2010; Collin *et al.*, 2011b; Tulldahl and Wikström, 2012).

As a result of this first mission with the Chiroptera II in Maritime Canada, several important things have been learned and demonstrated. The existence of five coastal study sites to survey during the mission provided flexibility to optimize where to survey based on the best water clarity conditions. The turbidity management approach used during the mission can be improved with additional sensors that measure water clarity or turbidity in combination with atmospheric drivers such as wind speed and direction. Ideally, to be able to access these in situ sensors remotely to determine if the conditions are acceptable for a TBL survey would be ideal; however, that may be too costly at the present time. Until real-time sensors that can be accessed remotely are affordable, building up a knowledge of the area through the collection of time-series of data related to turbidity and weather can add to operational efficiency. For most of the coastal sites along the Northumberland Strait, 6-m depth was achieved.

Some of the applications of TBL data for the survey sites listed in this paper have been presented. These include an empirical method to depth normalize the amplitude and produce a studywide seamless image mosaic of amplitude that can be visually interpreted on its own or combined with elevation data to generate hybrid image products. The depth-normalized amplitude image may be suitable for input into seabed classification, which will be a focus of future research. Depth-derived variables representing rugosity as a measure of eelgrass were used, and the eelgrass map has been simplified to a presence absence map with 80% agreement to ground truth data. Finally, efforts to optimize lidar data collection by using environmental data to monitor turbidity have been described.

LITERATURE CITED

Airborne Hydrography AB, 2014. Chiroptera II. http://www.airbornehydro.com/chiroptera-ii.

Allouis, T.; Bailly, J.-S.; Pastol, Y., and Le Roux, C., 2010. Comparison of LiDAR waveform processing methods for very shallow water bathymetry using Raman, near-infrared and green signals. *Earth Surface Processes and Landforms,* 35, 640–650. doi:10.1002/esp.1959.

AMEC Earth & Environmental, 2007. Northumberland Strait Ecosystem Overview Report Moncton, New Brunswick (Submitted to Fisheries and Oceans Canada No. TE61035). Moncton, NB.

Arifin, R.R. and Kennedy, A.B., 2011. The evolution of large scale crescentic bars on the northern Gulf of Mexico coast. *Marine Geology,* 285, 46–58. doi:10.1016/j.margeo.2011.04.003.

Bouhdaoui, A.; Bailly, J.-S.; Baghdadi, N., and Abady, L., 2014. Modeling the water bottom geometry effect on peak time shifting in LiDAR bathymetric waveforms. *IEEE Geoscience and Remote Sensing Letters,* 11, 1285–1289. doi:10.1109/LGRS.2013.2292814.

Brock, J.C. and Purkis, S.J., 2009. The emerging role of lidar remote sensing in coastal research and resource management. *In:* Brock, J.C. and Purkis, S.J. (eds.), *Coastal Applications of Airborne Lidar. Journal of Coastal Research*, Special Issue No. 53, pp. 1–5.

Brock, J.C.; Wright, C.W.; Kuffner, I.B.; Hernandez, R., and Thompson, P., 2006. Airborne lidar sensing of massive stony coral colonies on patch reefs in the northern Florida reef tract. *Remote Sensing of Environment,* 104, 31–42. doi:10.1016/j.rse.2006.04.017.

Chust, G.; Grande, M.; Galparsoro, I.; Uriarte, A., and Borja, Á., 2010. Capabilities of the bathymetric Hawk Eye LiDAR for coastal habitat mapping: A case study within a Basque estuary. *Estuarine, Coastal and Shelf Science,* 89, 200–213. doi:10.1016/j.ecss.2010.07.002.

Collin, A.; Archambault, P., and Long, B., 2011. Predicting species diversity of benthic communities within turbid nearshore using full-waveform bathymetric LiDAR and machine learners. *PloS One 6,* e21265. doi:10.1371/journal.pone.0021265.

Collin, A.; Long, B., and Archambault, P., 2011. Benthic classifications using bathymetric LIDAR waveforms and integration of local spatial statistics and textural features. *In*: Pe'eri, S. and Long, B. (eds.), *Applied LIDAR Techniques. Journal of Coastal Research*, Special Issue No. 62, pp. 86–98. doi:10.2112/SI_62_9.

Collin, A.; Long, B., and Archambault, P., 2012. Merging land-marine realms: Spatial patterns of seamless coastal habitats using a multispectral LiDAR. *Remote Sensing of Environment,* 123, 390–399. doi:10.1016/j.rse.2012.03.015.

Elhassan, I., 2015. Development of bathymetric techniques. *International Federation of Surveyors Working Week 2015: From the Wisdom of the Ages to the Challenges of the Modern World* (Sofia, Bulgaria).

Fisheries and Oceans Canada, 2008. Economic Impact of Marine Related Activities in Canada. http://www.dfo-mpo.gc.ca/ea-ae/cat1/no1-1/no1-1-eng.htm.

Fisheries and Oceans Canada, 2009. Does Eelgrass (Zostera marina) meet the criteria as an ecologically significant species? *Canadian Science Advisory Secretariat Science Advisory Report No. 2009/018*. Fisheries and Oceans Canada, Science, Gulf Region.

Forbes, D.L.; Manson, G.K.; Charles, J.; Thompson, K.R., and Taylor, R.B., 2009. *Halifax Harbour Extreme Water Levels in*

the Context of Climate Change: Scenarios for a 100-Year Planning Horizon. Geological Survey of Canada, Open File No. 6346, 22p.

Hanson, A.R., 2004. *Status and Conservation of Eelgrass (Zostera marina) in Eastern Canada. Technical Report Series No. 412*, Canadian Wildlife Service, Environmental Conservation Branch, Atlantic Region.

Kennedy, A.B.; Slatton, K.C.; Hsu, T.-J.; Starek, M.J., and Kampa, K., 2008. Ephemeral sand waves in the hurricane surf zone. *Marine Geology,* 250, 276–280. doi:10.1016/j.margeo.2008.01.015.

Nayegandhi, A.; Brock, J.C., and Wright, C.W., 2009. Small-footprint, waveform-resolving lidar estimation of submerged and sub-canopy topography in coastal environments. *International Journal of Remote Sensing,* 30, 861–878. doi:10.1080/01431160802395227.

Paine, J.G.; Andrews, J.R.; Saylam, K., and Tremblay, T.A., 2015. Airborne LiDAR-Based Wetland and Permafrost-Feature Mapping on an Arctic Coastal Plain, North Slope, Alaska. *In*: Tiner, R.W.; Lang, M.W., and Klemas, V.V. (eds.), *Remote Sensing of Wetlands: Applications and Advances.* Boca Raton, FL: CRC Press, pp. 413–434.

Peltier, W.R., 2004. Global glacial isotasy and the surface of the Ice-Age Earth: The ICE-5G (VM2) Model and GRACE. *Annual Review of Earth and Planetary Sciences,* 32, 111–149. doi:10.1146/annurev.earth.32.082503.144359.

Rahmstorf, S.; Cazenave, A.; Church, J.A.; Hansen, J.E.; Keeling, R.F.; Parker, D.E., and Somerville, R.C.J., 2007. Recent climate observations compared to projections. *Science,* 316, 709–709. doi:10.1126/science.1136843.

Reif, M.K.; Wozencraft, J.M.; Dunkin, L.M.; Sylvester, C.S., and Macon, C.L., 2013. A review of U.S. Army Corps of Engineers airborne coastal mapping in the Great Lakes. *Journal of Great Lakes Research,* 39, Supplement 1, 194–204. doi:10.1016/j.jglr.2012.11.002.

Sebert, L. and Munro, M.R., 1972. *Dimensions and Areas of maps of the National Topographic System of Canada.* Ottawa, ON: Department of Energy, Mines, and Resources, Surveys and Mapping, Technical Report 72-1, 29p.

Shachak, P.; McLeod, A.; Lavoie, P.; Ackerman, S.; Gardner, J., and Parrish, C., 2013. Field calibration and validation of remote-sensing surveys. *International Journal of Remote Sensing,* 34, 6423–6436. doi:10.1080/01431161.2013.800655.

Shaw, J.; Taylor, R.B.; Forbes, D.L.; Ruz, M.-H., and Solomon, S., 1998. *Sensitivity of the Coasts of Canada to Sea-level Rise. Geological Survey of Canada Bulletin No. Bulletin 505.*

Natural Resources Canada.

Stocker, T.F.; Qin, D.; Plattner, G.K.; Tignor, M.; Allen, S.K.; Boschung, J.; Nauels, A.; Xia, Y.; Bex, V., and Midgley, P.M. (Eds.), 2013. IPCC. Summary for Policymakers. *In*: *Climate Change 2013: The Physical Science Basis, Contribution of Working Group I to the Fifth Assessment Report of the Intergovernmental Panel on Climate Change.* Cambridge, UK: Cambridge University Press, pp. 1–29.

Tedsen, E.; Boteler, B.; McGlade, K.; Srebotnjak, T., and Abhold, K., 2014. Marine Resource Management and Coastal Livelihoods: An Atlantic Perspective. Atlantic Future, Scientific Paper 15, http://www.ecologic.eu/11478.

Tulldahl, H.M. and Wikström, S.A., 2012. Classification of aquatic macrovegetation and substrates with airborne lidar. *Remote Sensing of Environment,* 121, 347–357. doi:10.1016/j.rse.2012.02.004.

Velasco, J.; Molina, I.; Martinez, E.; Arquero, A., and Prieto, J.F., 2014. Sea bottom classification by means of bathymetric LIDAR data. *IEEE Latin America Transactions,* 12, 590–595. doi:10.1109/TLA.2014.6868859.

Waddington, T. and Hart, K., 2003. *Tools and techniques for the acquisition of estuarine benthic habitat data. SAIC Report No. 628.* NOAA Coastal Services Center, 63p.

Wang, C.-K. and Philpot, W.D., 2007. Using airborne bathymetric lidar to detect bottom type variation in shallow waters. *Remote Sensing of Environment,* 106, 123–135. doi:10.1016/j.rse.2006.08.003.

Wang, C.-K.; Philpot, W.; Kim, M., and Lei, H.-M., 2011. A Monte Carlo study of the seagrass-induced depth bias in bathymetric lidar. *Optics Express,* 19, 7230–7243.

Wang, C.; Li, Q.; Liu, Y.; Wu, G.; Liu, P., and Ding, X., 2015. A comparison of waveform processing algorithms for single-wavelength LiDAR bathymetry. *ISPRS Journal of Photogrammetry and Remote Sensing,* 101, 22–35. doi:10.1016/j.isprsjprs.2014.11.005.

Wedding, L.M.; Friedlander, A.M.; McGranaghan, M.; Yost, R.S., and Monaco, M.E., 2008. Using bathymetric lidar to define nearshore benthic habitat complexity: Implications for management of reef fish assemblages in Hawaii. *Remote Sensing of Environment,* 112, 4159–4165. doi:10.1016/j.rse.2008.01.025.

Zavalas, R.; Ierodiaconou, D.; Ryan, D.; Rattray, A., and Monk, J., 2014. Habitat classification of temperate marine macroalgal communities using bathymetric LiDAR. *Remote Sensing,* 6, 2154–2175. doi:10.3390/rs6032154.